

See discussions, stats, and author profiles for this publication at: <https://www.researchgate.net/publication/231305854>

Structural, Mössbauer, and EPR investigations on two oxidation states of a five-coordinate, high-spin synthetic heme. Quantitative interpretation of zero-field parameters and large...

ARTICLE *in* INORGANIC CHEMISTRY · MAY 1992

Impact Factor: 4.76 · DOI: 10.1021/ic00036a023

CITATIONS

45

READS

15

9 AUTHORS, INCLUDING:



Xiao-Qi Ding

Hannover Medical School

59 PUBLICATIONS 803 CITATIONS

SEE PROFILE



Abbasher M. Gismelseed

Sultan Qaboos University

94 PUBLICATIONS 439 CITATIONS

SEE PROFILE



A. X. Trautwein

Universität zu Lübeck

561 PUBLICATIONS 9,876 CITATIONS

SEE PROFILE



Habib Nasri

University of Monastir

64 PUBLICATIONS 752 CITATIONS

SEE PROFILE

Contribution from the Institut für Physik, Medizinische Universität zu Lübeck, Ratzeburger Allee 160, W-2400 Lübeck, FRG, and Laboratoire de Cristalchimie et de Chimie Structurale, URA (CNRS) 424, Institut le Bel, Université Louis Pasteur, 4 Rue Blaise Pascal, F-67070 Strasbourg, France

Structural, Mössbauer, and EPR Investigations on Two Oxidation States of a Five-Coordinate, High-Spin Synthetic Heme. Quantitative Interpretation of Zero-Field Parameters and Large Quadrupole Splitting

Emile L. Bominaar,^{†,‡} Xiao-Qi Ding,[†] Abbasher Gismelseed,^{†,§} Eckhard Bill,[†] Heiner Winkler,[†] Alfred X. Trautwein,^{*,†} Habib Nasri,[§] Jean Fischer,[§] and Raymond Weiss^{*,§}

Received May 22, 1991

The ferrous and ferric form of a ("picket-fence" porphyrinato)(acetato)iron complex, $[\text{Fe}^{\text{II/III}}(\text{CH}_3\text{CO}_2)(\text{TPpivP})]^{-0}$, were synthesized and characterized by UV-visible, ^1H NMR, EPR, and Mössbauer spectroscopy. The structure of the ferrous complex was determined by X-ray diffraction. Crystal data at -100°C : $[\text{Fe}^{\text{II}}(\text{CH}_3\text{CO}_2)(\text{TPpivP})][\text{NaC}_{22}\text{H}_{22}\text{Cl}(\text{C}_{90}\text{H}_{108}\text{N}_{10}\text{O}_{12})\cdot\text{NaCl}(\text{Fe})]$; monoclinic; $a = 18.040$ (5), $b = 21.521$ (5), $c = 22.605$ (5) Å; $\beta = 100.37$ (5) $^\circ$; $Z = 4$, $D_{\text{calc}} = 1.259$ g cm $^{-3}$; space group $P2_1/n$. The five-coordinate iron atom is bonded to four porphyrinato nitrogens ($\text{Fe}-\text{N}_p = 2.107$ (14) Å) and to an oxygen atom of the acetate ion ($\text{Fe}-\text{O}_{\text{acetate}} = 2.034$ (3) Å), placed inside the molecular cavity of the picket-fence porphyrin. Mössbauer spectra were recorded in the two oxidation states of the complex at temperatures varying from 1.5 to 200 K in fields of 0–6.21 T. The ferrous complex has a large quadrupole splitting, $\Delta E_Q = 4.25$ mm s $^{-1}$, nearly independent of temperature. In the ferric species, the quadrupole splitting, $\Delta E_Q = 1.1$ mm s $^{-1}$, is as normally found in ferric high-spin iron porphyrins. The spin-Hamiltonian analysis of the spectra yields the zero-field parameters $D = -0.9$ cm $^{-1}$ and $E/D = 0.33$ and the magnetic hyperfine parameters $A_{xy} = -17$ T and $A_z = -13.3$ T in the ferrous complex (spin $S = 2$) and $D = 7.5$ cm $^{-1}$, $E/D \approx 0$ and $A_{xy,z} = -20$ T in the ferric species ($S = 5/2$). The values of the zero-field parameters of the ferric species are confirmed by EPR analysis; the g values are $g_x = 1.960$, $g_y = 2.017$, and $g_z = 2.00$. The zero-field splittings and effective g values in the ferric complex are interpreted in terms of a crystal-field model. Theoretical estimates of the quadrupole splitting and zero-field parameters in the ferrous complex are given on the basis of molecular-orbital calculations. The relation between the zero-field tensor (\mathbf{D}) and electronic and X-ray structure in the ferrous species is discussed.

1. Introduction

Parallel to the discovery of the unusually large quadrupole splitting, $\Delta E_Q \approx 4$ mm s $^{-1}$, in the ferrous state of the prosthetic group termed P460 of the multiheme enzyme hydroxylamine oxidoreductase from the bacterium *Nitrosomonas europaea*,^{1,2} comparably large splittings were observed in a number of synthetic five-coordinate porphyrins of the formula $[\text{Fe}(\text{X})(\text{Porph})]^-$, where X is an anionic oxygen- or nitrogen-donor ligand or a halide ion.^{3–8} In order to gain more insight into the electronic structure of the iron ions in these complexes, field- and temperature-dependent Mössbauer measurements have been performed in the synthetic phenolato porphyrinato complex $[\text{Fe}^{\text{II}}(\text{OC}_6\text{H}_5)(\text{TPP})]^-$ by Lang et al.⁸ For the derivation of a set of zero-field parameters consistent with both the susceptibility and Mössbauer data in the phenolate complex, these authors introduced weak antiferromagnetic exchange coupling between the paramagnetic iron centers.⁸ Strong correlations between the sign and magnitude of the zero-field parameter D and the value of the exchange-coupling constant were found in the simulations of the magnetic susceptibility data. However, the spin-Hamiltonian parameters inferred from the Mössbauer spectra are rather insensitive to the weak intermolecular couplings. The value of the zero-field parameter D obtained by Lang et al. is small and negative (see Table I). The principal components of the magnetic hyperfine tensor (\mathbf{A}) in the complex are negative, which is characteristic of a dominant Fermi contact interaction. Furthermore, the \mathbf{A} tensor shows anisotropy, $|A_z| < |A_{xy}|$, originating from spin-dipolar interaction. The anisotropy of the \mathbf{A} tensor and the positive sign of the main component of the electric-field-gradient (EFG) tensor indicate that the iron(II) ion in the phenolate complex possesses a half-filled subshell of spin-parallel electrons plus an "excess" electron of opposite spin in an oblate orbital of d_{xy} type.^{8,9} The weak temperature dependence of the quadrupole splitting in the range 1–300 K shows that the ground orbital state is energetically well-separated from excited orbital states by energy gaps typically 1 order

Table I. Spin-Hamiltonian Parameters Deduced from the Mössbauer Data of the Ferrous High-Spin ($S = 2$) Complexes $[\text{Fe}^{\text{II}}(\text{OC}_6\text{H}_5)(\text{TPP})]^-$ and $[\text{Fe}^{\text{II}}(\text{CH}_3\text{CO}_2)(\text{TPpivP})]^-$

	$[\text{Fe}(\text{OC}_6\text{H}_5)(\text{TPP})]^-$ ^a	$[\text{Fe}(\text{CH}_3\text{CO}_2)(\text{TPpivP})]^-$ ^a
ΔE_Q , mm s $^{-1}$	+4.01 ^b	+4.25 ^b
η	0 ^c	0 ^c
δ , mm s $^{-1}$	1.03 ^{b,d}	1.05 ^{b,d}
Γ , mm s $^{-1}$	0.25 ^b	0.40 ^b
g_x	2 ^c	2 ^c
g_y	2 ^c	2 ^c
g_z	2 ^c	2 ^c
A_x , T	-17.6	-17.0
A_y , T	-17.6	-17.0
A_z , T	-12.8	-13.3
D , cm $^{-1}$	-1.6	-0.9
E/D	0 ^c	0.333 ^e
α, β, γ , deg	0 ^{c,f}	0 ^{c,f}

^a Present work. ^b Measured at 4.2 K. ^c Not varied in the simulations.

^d Relative to α -Fe at room temperature. ^e Real value may be smaller (see text). ^f Euler angles taking principal axes of \mathbf{D} tensor into those of EFG tensor.

of magnitude larger than the spin-orbit coupling interaction, which is a prerequisite for the applicability of spin-Hamiltonian analysis.

In this paper, the syntheses of the ferrous and ferric forms of the (acetato)iron "pivalamide-picket-fence" porphyrin, $[\text{Fe}^{\text{II/III}}(\text{CH}_3\text{CO}_2)(\text{TPpivP})]^{-0}$, are reported, together with the X-ray structure of the ferrous form. The spin-Hamiltonian analysis of the Mössbauer spectra in the ferrous species, reported earlier in a short conference note,⁹ is reexamined, thereby adopting from the beginning collinearity of the principal axes of the EFG, \mathbf{A} , \mathbf{D} , and \mathbf{g} tensors. EPR spectra and Mössbauer spectra recorded at

[†] Medizinische Universität zu Lübeck.

[‡] Present address: Laboratoire de Chimie Inorganique, Université de Paris-Sud, Bat. 420, 91405 Orsay, France.

[§] Université Louis Pasteur.

^{*} Present address: Department of Physics, University of Khartoum, Khartoum, Sudan.

- (1) Anderson, K. K.; Kent, T. A.; Lipscomb, J. D.; Hooper, A. B.; Münck, E. *J. Biol. Chem.* **1984**, *259*, 6833.
- (2) Prince, R. C.; Hooper, A. B. *Biochemistry* **1987**, *26*, 970.
- (3) Schappacher, M.; Ricard, L.; Weiss, R.; Montiel-Montoya, R.; Gonser, U.; Bill, E.; Trautwein, A. X. *Inorg. Chim. Acta* **1983**, *78*, L9.
- (4) Silver, J.; Luckas, B. *Inorg. Chim. Acta* **1983**, *80*, 107.
- (5) Silver, J.; Luckas, B.; Al-Jaff, G. *Inorg. Chim. Acta* **1984**, *91*, 125.
- (6) Nasri, H.; Fischer, J.; Weiss, R.; Bill, E.; Trautwein, A. X. *J. Am. Chem. Soc.* **1987**, *109*, 2549.
- (7) Shaevitz, B. A.; Lang, G.; Reed, C. A. *Bull. Am. Phys. Soc.* **1987**, *32*, 411.
- (8) Shaevitz, B. A.; Lang, G.; Reed, C. A. *Inorg. Chem.* **1988**, *27*, 4607.
- (9) Bill, E.; Gismelseed, A.; Laroque, D.; Trautwein, A. X.; Fischer, J.; Weiss, R. *Hyperfine Interact.* **1988**, *42*, 881.

various temperatures and magnetic fields in the ferric species are also analyzed by the spin-Hamiltonian method. For the interpretation of the spin-Hamiltonian parameters, we performed a self-consistent-charge linear-combination-of-atomic-orbital molecular-orbital (MO) calculation in the ferrous species, as defined by its X-ray structure. Theoretical estimates of the quadrupole splitting and the zero-field parameters are given on the basis of the MO results. The dependences of the zero-field parameters on the electronic structure of the 3d shell of iron in the ferrous and ferric species are discussed. The effect of distortions from C_{4v} symmetry in the first ligand shell of the iron ion in the ferrous complex on zero-field parameters is systematically analysed in the framework of a crystal-field model.

2. Experimental Section

All preparations were carried out in Schlenk tubes under argon. Pentane was dried by distillation over CaH_2 . Benzene was degassed and dried by distillation over sodium/benzophenone; chlorobenzene was purified by distillation over P_2O_5 . Acetic acid, acetic anhydride, and sodium acetate were obtained from Aldrich and used without further purification. The free *meso*-tetrakis($\alpha,\alpha,\alpha,\alpha$ -*o*-pivalamidophenyl)porphyrin and corresponding chloroiron(III) derivative were synthesized by methods given in the literature.¹⁰ The six-coordinate (triflate)quoiron(III) picket-fence porphyrin complex was prepared by metathesis of the ferric chloro compound with the silver salt of triflic acid, according to our procedure described elsewhere.¹⁰

2.1. Synthesis of $[\text{Fe}^{\text{II}}(\text{CH}_3\text{CO}_2)(\text{TPpivP})][\text{NaC}222]\cdot\text{C}_6\text{H}_5\text{Cl}$. Dry, deoxygenated chlorobenzene was added, under argon, to a mixture of $[\text{Fe}^{\text{III}}(\text{CF}_3\text{SO}_3)(\text{H}_2\text{O})(\text{TPpivP})]$ (25 mg, 0.02 mmol) and zinc amalgam. The resulting blood-red solution was stirred under argon for 1 h. Then, a chlorobenzene solution (10 mL) containing a large excess of sodium acetate (26 mg, 0.32 mmol) was added under continuous swirling followed, subsequently, by Kryptofix 222 (76 mg, 0.2 mmol), and the resulting solution was again stirred for 1 h. It was then filtered, and dry, degassed pentane was slowly added (50 mL). This mixture was set aside for crystallization at -5°C .

UV-visible: $\lambda_{\text{max}}(\text{C}_6\text{H}_5\text{Cl}) = 448, 572, 611 \text{ nm}$.

2.2. Synthesis of $[\text{Fe}^{\text{III}}(\text{CH}_3\text{CO}_2)(\text{TPpivP})]$. A solution of KOH (13.72 g, 245 mmol) in water (35 mL) was added to a solution of $[\text{Fe}^{\text{III}}(\text{CF}_3\text{SO}_3)(\text{H}_2\text{O})(\text{TPpivP})]$ (150 mg, 122 mmol) in benzene (50 mL). After being stirred for 2 h, the solution was set aside for one night. It was then filtered, and acetic acid (12 mL) and acetic anhydride (6 mL) were added; the mixture was stirred for 1 h and evaporated under vacuum. The resulting solid was dried under vacuum at 35°C for 24 h.

Anal. Calcd for $\text{C}_{66}\text{H}_{67}\text{N}_9\text{O}_6\text{Fe}$: C, 70.55; H, 5.96; N, 9.97. Found: C, 70.64; H, 6.08; N, 9.83.

UV-visible: $\lambda_{\text{max}}(\text{C}_6\text{H}_5\text{Cl}) = 344, 414, 505, 574, 645 \text{ nm}$. ^1H NMR (toluene- d_6): $\delta(\text{H}_{\text{pyrr}}) = 78.1 \text{ ppm/TMS}$.

2.3. X-ray Crystallography. Suitable single crystals of $[\text{Fe}^{\text{II}}(\text{CH}_3\text{CO}_2)(\text{TPpivP})][\text{NaC}222]\cdot\text{C}_6\text{H}_5\text{Cl}$ were obtained by slow diffusion of chlorobenzene solutions of the complex into pentane at -5°C . A systematic search in reciprocal space using a Philips PW1100/16 automatic diffractometer showed that the crystals belong to the monoclinic system.

Quantitative data were obtained at -100°C using a locally built gas-flow device. All experimental parameters used are given in Table II. The resulting data set was transferred to a VAX computer, and for all subsequent calculations the Enraf-Nonius SDP/VAX package¹¹ was used, with the exception of a local data-reduction program.

Three standard reflections measured every hour during the entire data-collection period showed no significant trend. The raw step-scan data were converted to intensities using the Lehmann-Larsen method¹² and then corrected for Lorentz and polarization factors.

The structure was resolved using the heavy-atom method. After refinement of the heavy-atom positions, a Fourier-difference map revealed maxima of residual electron density close to the positions expected for the hydrogen atoms; they were introduced in the structure-factor calculations by their computed coordinates ($\text{C}-\text{H} = 0.95 \text{ \AA}$) and isotropic temperature factors such as $B(\text{H}) = 1.3B_{\text{eq}}(\text{C}) \text{ \AA}^2$, but were not refined. The five hydrogen atoms of the solvent molecule were omitted. At this

Table II. X-ray Experimental Parameters

formula	$\text{C}_{90}\text{H}_{108}\text{N}_{10}\text{O}_{12}\cdot\text{NaClFe}$	temp, $^\circ\text{C}$	-100
mol wt	1636.21	diffractometer	Philips PW 1100/16
color	dark blue	mode	$\theta/2\theta$ flying step-scan
cryst syst	monoclinic	scan speed, deg^{-1}	0.024
a , \AA	18.040 (5)	scan width, deg	$1.20 + 0.143(\tan \theta)$
b , \AA	21.521 (5)	step width, deg	0.05
c , \AA	22.605 (5)	θ limits, deg	4–57
β , deg	100.37 (2)	octants	$\pm h, \pm k, \pm l$
V , \AA^3	8632.8	no. of data colld	12111
Z	4	no. of data with	7337
D_{calc} , g cm^{-3}	1.259	$I > 3\sigma(I)$	
space group	$P2_1/n$	abs min/max	0.74/1.13
radiation	$\text{Cu K}\alpha$ (graphite monochromated)	$R(F)$	0.077
wavelength, \AA	1.5418	$R_w(F)$	0.118
μ , cm^{-1}	22.536	p	0.08
cryst size mm	$0.22 \times 0.34 \times 0.38$	GOE	1.507

stage, before anisotropic refinements were undertaken, empirical absorption corrections were applied (Fourier method, program DIFABS¹³) using the method of Walker and Stuart,¹³ since face indexation was not possible under a cold gas stream and the air sensitivity of the crystals under normal atmosphere at room temperature. Immediate improvement of the $R(F)$ factor was 1.3%. Full least-squares refinements were performed using the weighting scheme $\sigma^2(F^2) = \sigma^2_{\text{counts}} + (p/I)^2$, with a quite large fudge factor p of 0.08 since, as is often the case in picket-fence porphyrin complexes and [222] cryptates, one of the pivalamide "pickets" of the porphyrinato anion and one of the polyether chains of the cryptate cation show residual disorder and/or high thermal motion. This is also true for the chlorobenzene solvate molecule present in $[\text{Fe}(\text{CH}_3\text{CO}_2)(\text{TPpivP})][\text{NaC}222]\cdot\text{C}_6\text{H}_5\text{Cl}$. No extinction corrections were applied since the plot of $I_{\text{cal}}/I_{\text{obs}}$ versus I_{cal} has an intercept of 0.99 and a slope of 1.01×10^{-6} . The final difference map revealed no significant maxima. The scattering-factor coefficients and anomalous dispersion coefficients were taken from ref 14.

2.4. Spectroscopic Methods. UV-visible spectra were obtained with a Cary 210 spectrometer. The ^1H NMR spectra of $[\text{Fe}^{\text{II/III}}(\text{CH}_3\text{CO}_2)(\text{TPpivP})]^{-/0}$ were measured on a Bruker SY 200 instrument.

The Mössbauer spectrometer works in conventional constant-acceleration mode with a source of 1.85 GBq $^{57}\text{Co}/\text{Rh}$ (Amersham Buchler). From calibration measurements we obtained a standard line width of 0.23 mm s^{-1} . Isomer shifts are given relative to metallic iron ($\alpha\text{-Fe}$) at room temperature. Low-temperature Mössbauer measurements were performed in a helium-bath cryostat (MD306, Oxford Instruments) and a system with a superconducting magnet (Oxford Instruments). Small fields of 20 mT were applied to the tail of the bath cryostat with the help of a permanent magnet.

The EPR spectrometer was a conventional X-band apparatus (Bruker ER200D); the data acquisition system, based on a personal computer, is a local development. The spectrometer was equipped with a helium-flow cryostat (Oxford Instruments ESR 910), which provides temperatures down to 2.5 K.

3. Results

3.1. X-ray Structure of $[\text{Fe}^{\text{II}}(\text{CH}_3\text{CO}_2)(\text{TPpivP})][\text{NaC}222]\cdot\text{C}_6\text{H}_5\text{Cl}$. The asymmetric units of the crystals contain one formula unit, $[\text{Fe}(\text{CH}_3\text{CO}_2)(\text{TPpivP})][\text{NaC}222]\cdot\text{C}_6\text{H}_5\text{Cl}$. Table III lists the positional parameters of all non-hydrogen atoms of the $[\text{Fe}^{\text{II}}(\text{CH}_3\text{CO}_2)(\text{TPpivP})]^{-}$ anion. The acetate anionic axial ligand is located inside the molecular cavity of the picket-fence porphyrin (Figure 1). This is the usual geometry in five-coordinate, high-spin iron(II) picket-fence porphyrin complexes with anionic axial ligands.^{3,6,15,16} The $\text{Fe}-\text{N}_p$ bond lengths (Table IV) range from 2.089 (3) to 2.122 (3) \AA . The corresponding mean value is 2.107 (14) \AA . The iron atom lies considerably out of the 4N_p and 24-atom-core mean planes. The out-of-plane displacements relative to these planes are $\Delta(4\text{N}_p) = 0.55$ (1) \AA and $\Delta(\text{core}) = 0.64$ (1) \AA , respectively. The $\text{Fe}-\text{O}$ axial bond length of 2.034

(10) Gismelseed, A.; Bominaar, E. L.; Bill, E.; Trautwein, A. X.; Winkler, H.; Nasri, H.; Doppelt, P.; Mandon, D.; Fischer, J.; Weiss, R. *Inorg. Chem.* **1990**, *29*, 2741.

(11) Frenz, B. A. The Enraf-Nonius CAD4-SDP. In *Computing in Crystallography*; Schenk, H., Olthof-Hazekamp, R., Van Koningsveld, H., Bassi, G. C., Eds.; Delft University Press: Delft, The Netherlands, 1978; pp 64–71.

(12) Lehmann, M. S.; Larsen, F. K. *Acta Crystallogr.* **1974**, *A30*, 580.

(13) Walker, N.; Stuart, D. *Acta Crystallogr.* **1983**, *A39*, 158.

(14) Cromer, D. T.; Waber, J. T. *International Tables for X-ray Crystallography*; The Kynoch Press: Birmingham, England, 1983; Vol. IV: (a) Table 2.2b; (b) Table 2.3.1.

(15) Schappacher, M.; Ricard, L.; Fischer, J.; Weiss, R.; Montiel-Montoya, R.; Bill, E.; Trautwein, A. X. *Inorg. Chem.* **1989**, *28*, 4639.

(16) Bounab, B.; Ricard, L.; Fischer, J.; Weiss, R. To be published.

Table III. Positional Parameters and Their Esd's for $[\text{Fe}(\text{CH}_3\text{CO}_2)(\text{TPpivP})]^-$

atom	x	y	z	$B, \text{\AA}^2$	atom	x	y	z	$B, \text{\AA}^2$
Fe	0.45962 (5)	0.06958 (4)	0.76655 (4)	2.15 (2)	C40	0.7636 (5)	0.1459 (4)	1.0102 (4)	4.8 (2)
N1	0.3737 (3)	0.0059 (2)	0.7721 (2)	2.2 (1)	C41	0.8311 (5)	0.1463 (4)	0.9889 (4)	4.5 (2)
C2	0.2992 (4)	0.0112 (3)	0.7468 (3)	2.4 (1)	C42	0.8333 (4)	0.1258 (4)	0.9308 (4)	4.0 (2)
C3	0.2631 (4)	-0.0484 (3)	0.7465 (3)	2.9 (1)	C43	0.7682 (4)	0.1054 (3)	0.8935 (3)	3.2 (2)
C4	0.3157 (4)	-0.0892 (3)	0.7719 (3)	2.6 (1)	N44	0.7650 (3)	0.0866 (3)	0.8332 (3)	3.5 (1)
C5	0.3851 (3)	-0.0547 (3)	0.7889 (3)	2.2 (1)	C45	0.8208 (4)	0.0806 (4)	0.8019 (4)	4.1 (2)
C6	0.4523 (3)	-0.0790 (3)	0.8210 (3)	2.1 (1)	O46	0.8864 (3)	0.0892 (4)	0.8222 (3)	7.2 (2)
C7	0.5183 (3)	-0.0454 (3)	0.8436 (3)	2.2 (1)	C47	0.7965 (4)	0.0604 (4)	0.7353 (4)	4.1 (2)
C8	0.5831 (4)	-0.0686 (3)	0.8832 (3)	2.6 (1)	C48	0.8378 (6)	0.0000 (5)	0.7263 (5)	6.9 (3)
C9	0.6305 (4)	-0.0211 (3)	0.8997 (3)	2.7 (1)	C49	0.8243 (6)	0.1120 (5)	0.6974 (4)	6.3 (2)
C10	0.5955 (3)	0.0331 (3)	0.8684 (3)	2.2 (1)	C50	0.7119 (5)	0.0508 (5)	0.7158 (4)	5.9 (2)
N11	0.5277 (3)	0.0175 (2)	0.8342 (2)	2.2 (1)	C51	0.4523 (4)	0.2975 (3)	0.7281 (3)	3.0 (2)
C12	0.6259 (4)	0.0925 (3)	0.8724 (3)	2.6 (1)	C52	0.4372 (4)	0.3452 (3)	0.7632 (4)	3.8 (2)
C13	0.5936 (4)	0.1449 (3)	0.8397 (3)	2.8 (1)	C53	0.4433 (4)	0.4069 (3)	0.7462 (4)	3.9 (2)
C14	0.6273 (4)	0.2065 (3)	0.8434 (4)	3.8 (2)	C54	0.4655 (5)	0.4188 (3)	0.6925 (4)	4.4 (2)
C15	0.5801 (4)	0.2439 (3)	0.8080 (4)	3.6 (2)	C55	0.4799 (5)	0.3718 (4)	0.6550 (4)	4.5 (2)
C16	0.5156 (4)	0.2068 (3)	0.7828 (3)	2.8 (1)	C56	0.4732 (5)	0.3110 (3)	0.6723 (3)	4.0 (2)
N17	0.5250 (3)	0.1468 (2)	0.8021 (2)	2.3 (1)	N57	0.4905 (4)	0.2599 (3)	0.6380 (3)	5.3 (2)
C18	0.4493 (4)	0.2308 (3)	0.7479 (3)	2.6 (1)	C58	0.5075 (4)	0.2581 (4)	0.5831 (3)	3.7 (2)
C19	0.3825 (4)	0.1980 (3)	0.7300 (3)	2.4 (1)	O59	0.5076 (4)	0.3035 (3)	0.5527 (3)	6.0 (2)
C20	0.3126 (4)	0.2247 (3)	0.6998 (3)	3.1 (2)	C60	0.5223 (4)	0.1929 (4)	0.5606 (3)	3.6 (2)
C21	0.2601 (4)	0.1793 (3)	0.6959 (3)	2.8 (1)	C61	0.5834 (5)	0.1605 (4)	0.6061 (4)	4.9 (2)
C22	0.2979 (4)	0.1235 (3)	0.7217 (3)	2.5 (1)	C62	0.5480 (6)	0.1996 (5)	0.4994 (4)	6.0 (2)
N23	0.3733 (3)	0.1366 (2)	0.7415 (2)	2.2 (1)	C63	0.4493 (5)	0.1553 (4)	0.5528 (5)	5.5 (2)
C24	0.2631 (4)	0.0662 (3)	0.7239 (3)	2.4 (1)	C64	0.1799 (4)	0.0635 (3)	0.7025 (3)	2.6 (1)
C25	0.4510 (3)	-0.1464 (3)	0.8374 (3)	2.2 (1)	C65	0.1290 (4)	0.0826 (3)	0.7377 (3)	2.9 (1)
C26	0.4086 (4)	-0.1661 (3)	0.8802 (3)	2.9 (1)	C66	0.0518 (4)	0.0789 (3)	0.7183 (3)	3.3 (2)
C27	0.4003 (4)	-0.2273 (3)	0.8940 (3)	3.2 (2)	C67	0.0248 (4)	0.0578 (3)	0.6611 (4)	3.7 (2)
C28	0.4339 (4)	-0.2722 (3)	0.8630 (3)	3.3 (2)	C68	0.0725 (4)	0.0380 (4)	0.6236 (3)	3.6 (2)
C29	0.4768 (4)	-0.2552 (3)	0.8206 (3)	3.0 (2)	C69	0.1512 (4)	0.0407 (3)	0.6446 (3)	2.9 (1)
C30	0.4864 (3)	-0.1920 (3)	0.8073 (3)	2.4 (1)	N70	0.2039 (3)	0.0233 (3)	0.6076 (3)	3.3 (1)
N31	0.5301 (3)	-0.1748 (2)	0.7636 (2)	2.6 (1)	C71	0.1977 (4)	-0.0225 (4)	0.5678 (4)	4.1 (2)
C32	0.5943 (4)	-0.2044 (3)	0.7558 (3)	3.2 (2)	O72	0.1404 (4)	-0.0534 (3)	0.5531 (4)	8.2 (2)
O33	0.6184 (3)	-0.2487 (3)	0.7872 (3)	5.6 (1)	C73	0.2688 (5)	-0.0377 (4)	0.5418 (4)	4.6 (2)
C34	0.6337 (4)	-0.1813 (3)	0.7072 (3)	3.8 (2)	C74	0.3238 (5)	0.0175 (5)	0.5450 (4)	5.8 (2)
C35	0.7009 (5)	-0.2252 (5)	0.7035 (5)	7.5 (3)	C75	0.3069 (6)	-0.0928 (5)	0.5759 (5)	7.1 (3)
C36	0.6638 (5)	-0.1165 (4)	0.7232 (4)	4.7 (2)	C76	0.2435 (7)	-0.0570 (6)	0.4741 (5)	8.7 (3)
C37	0.5804 (5)	-0.1808 (4)	0.6473 (4)	5.2 (2)	OA	0.4938 (3)	0.0482 (2)	0.6880 (2)	3.1 (1)
C38	0.6991 (4)	0.1062 (3)	0.9141 (3)	2.8 (1)	OB	0.4905 (3)	-0.0551 (2)	0.6949 (2)	4.9 (1)
C39	0.6982 (4)	0.1259 (3)	0.9730 (4)	3.9 (2)	CA	0.5012 (4)	-0.0076 (3)	0.6692 (3)	3.6 (2)
					CB	0.5294 (5)	-0.0112 (4)	0.6093 (4)	4.9 (2)

^a Values for anisotropically refined atoms are given in the form of the isotropic equivalent displacement parameter defined as $(4/3)[a^2\beta(1,1) + b^2\beta(2,2) + c^2\beta(3,3) + ab(\cos \gamma)\beta(1,2) + ac(\cos \beta)\beta(1,3) + bc(\cos \alpha)\beta(2,3)]$

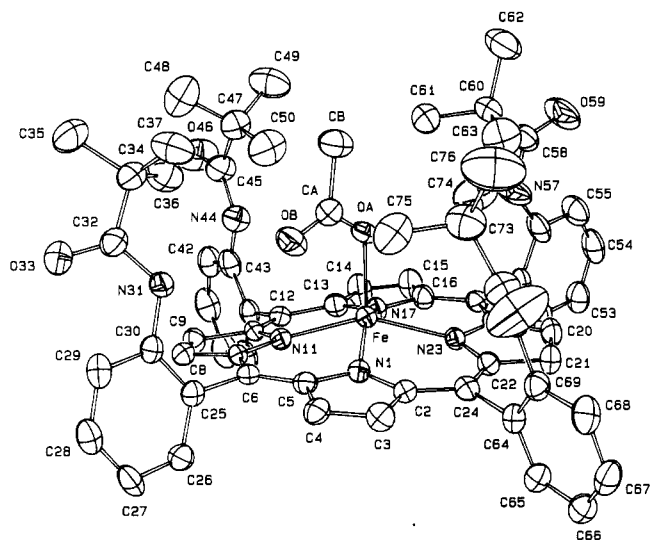


Figure 1. ORTEP plot of the ferrous complex $[\text{Fe}^{\text{II}}(\text{CH}_3\text{CO}_2)(\text{TPpivP})]^-$, showing part of the numbering scheme used. Ellipsoids are scaled to enclose 50% of the electron density. Hydrogen atoms are omitted.

(3) Å is somewhat elongated compared with the Fe–O axial bond distance of 1.937 (4) Å observed in the five-coordinate, high-spin iron(II) phenoxide picket-fence porphyrin derivative.⁶ The corresponding distances in the neutral, five-coordinate, high-spin iron(III) porphyrin complexes are 1.898 (4) Å (acetate) and 1.847

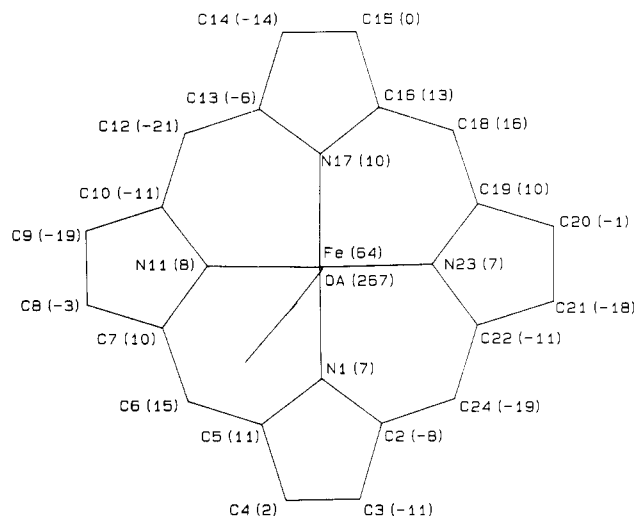


Figure 2. Stick-bond plot of the porphyrin ring showing the displacements, in units of 0.01 Å, of the atoms from their mean plane in the X-ray structure of the ferrous complex, $[\text{Fe}^{\text{II}}(\text{CH}_3\text{CO}_2)(\text{TPpivP})]^-$.

(2) Å (phenoxide).¹⁶ The acetate anion is hydrogen-bonded via its carbonyl group to the N31–H amido group of one "picket". The corresponding $\text{NH}\cdots\text{O}=\text{C}$ distance is 3.026 (5) Å. The Fe–O axial bond is slightly tipped away from the normal of the 4N_p mean plane by 1.4° and by 1.8° with respect to the normal of the 24-atom-core mean plane. As is shown in Figure 2, the porphyrin

Table IV. Selected Bond Lengths (Å), Bond Angles (deg), and Averages with their Estimated Standard Deviations

Fe-N1	2.089 (3)	N1-Fe-OA	104.4 (1)
Fe-N11	2.104 (3)	N11-Fe-OA	106.5 (1)
Fe-N17	2.112 (3)	N17-Fe-OA	105.9 (1)
Fe-N23	2.122 (3)	N23-Fe-OA	104.1 (1)
(Fe-N _p)	2.107 (14)		
Fe-OA	2.034 (3)		
Porphyrin^a			
N-C α	1.370 (9)	C α -N-C α	106.2 (3)
C α -C β	1.444 (8)	N-C α -C β	109.7 (6)
C β -C β	1.341 (9)	C α -C β -C β	107.1 (7)
C α -C m	1.399 (10)	N-C α -C m	125.1 (7)
C m -C p	1.502 (7)	C β -C α -C m	125.0 (6)
C p -Na	1.417 (6)	C α -C m -C α	125.7 (5)
Na-Ca1	1.338 (15)	C α -C m -C p	117 (2)
Ca1-Oa	1.211 (13)	C p -C p -C p	120 (1)
Ca1-Ca2	1.53 (2)		
Ca2-Ct	1.53 (2)		
Cryptate			
N-C	1.46 (2)	C-N-C	110 (1)
C-C	1.49 (2)	C-O-C	111 (1)
C-O	1.42 (2)		
Na...N77	3.115 (4)		
Na...N86	3.010 (4)		
Na...O	2.689 (4)-2.818 (3)		

^a C α , C β , C m and C p stand respectively for α , β , meso, and phenyl carbon atoms of the porphyrin macrocycle. Na, Oa, Ca and Ct stand respectively for nitrogen, oxygen, carbon amido atoms and *tert*-butyl carbon atoms.

ring has an irregular, domed conformation. The doming induces a separation of 0.08 Å between the 4N_p and the 24-atom-core mean planes. Despite the irregularity of the doming, the mean planes are almost parallel; their dihedral angle is only 0.47°. As usual, the pyrrole rings are almost planar. The dihedral angles between the mean pyrrole planes range from 1.3 to 15.0°, the mean value being 10.0°. The closest Fe-Fe separations between neighboring porphyrinato anions are all larger than 10 Å (10.81, 12.75, 13.09, ... Å). An ORTEP diagram showing the packing of porphyrinato anions, cryptate cations, and chlorobenzene solvate molecules in the unit cell of the crystals is provided in the supplementary material. It shows that the chlorobenzene solvate molecules do not lie between two porphyrinato anions and do not interact via their π electrons with the porphyrin macrocycles.

Agreements between chemically equivalent bond distances and angles within the porphyrin macrocycle, the pivalamide pickets, and the acetato anionic axial ligand are satisfactory. This agreement is slightly poorer in the cryptate cation and the chlorobenzene solvate molecule, since the average thermal motion of these entities is higher.

Figure 3 depicts the distortions from axial symmetry (C_{4v}) in the ligand shell of the iron ion. The symmetrized structure, with respect to which the distortions are defined, is constructed as follows. The origin of the coordinate axes, Ct, is taken at the center-of-gravity of the four N_p atoms. The orientation of the xy plane is defined by minimizing the sum of squares of the distances of the N_p atoms to this plane. The y axis is chosen through the projection of one of the N_p atoms on the xy plane. The labeling of the distortions in Figure 3 will be used in section 4.1 in a systematic analysis of the interdependence of zero-field parameters and structure.

3.2. Mössbauer Analysis of the Ferrous Complex. The Mössbauer spectra of a polycrystalline sample of the ferrous complex [Fe^{II}(CH₃CO₂)(TPpivP)]⁻ recorded without applied magnetic field in the temperature range 4.2–215 K consist of a symmetric quadrupole doublet with large, weakly temperature-dependent splitting, $\Delta E_Q(4.2\text{--}215\text{ K}) = 4.25\text{--}4.05\text{ mm s}^{-1}$, and with an isomer shift, $\delta(4.2\text{--}215\text{ K}) = 1.05\text{--}0.95\text{ mm s}^{-1}$, which is characteristic for high-spin ferrous iron. The spectra recorded in applied fields ranging from 60 mT to 6.21 T, at variable tem-

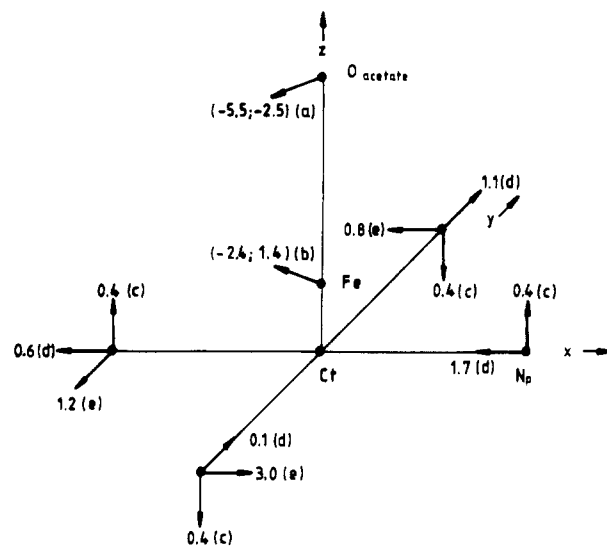


Figure 3. Cartesian components of the distortions, (a, ..., e), of the iron ion and its ligand shell, in units of 0.01 Å, from the symmetrized (C_{4v}) structure defined in the text, as obtained from the X-ray structure of the ferrous complex [Fe^{II}(CH₃CO₂)(TPpivP)]⁻. The arrows indicate the directions of the displacements. $R(\text{Ct-N}_p)_{\text{av}} = 2.034\text{ Å}$, $z(\text{O}_{\text{acetate}}) = 2.584\text{ Å}$, and $z(\text{Fe}) = 0.55\text{ Å}$.

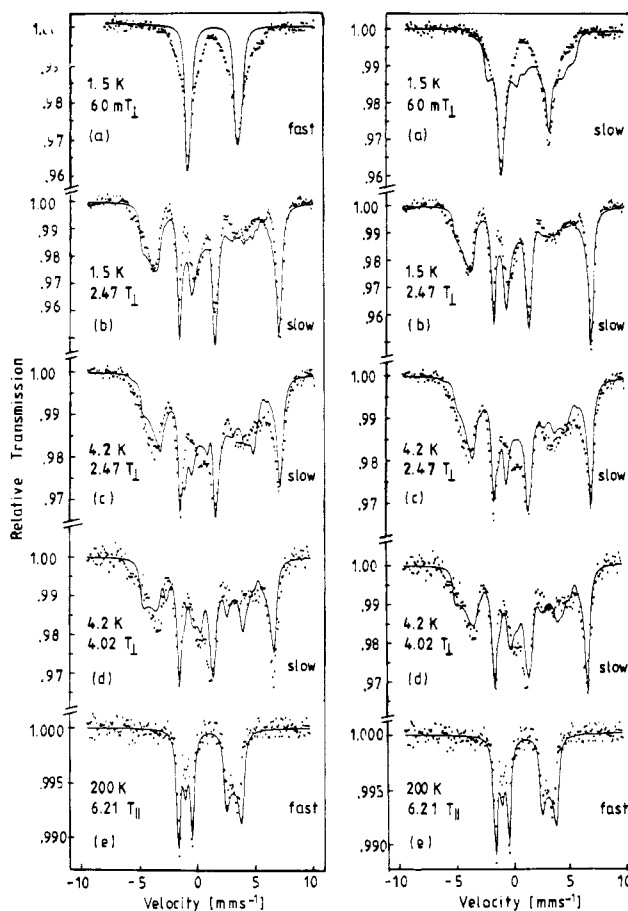


Figure 4. Mössbauer spectra of the ferrous complex [Fe^{II}(CH₃CO₂)(TPpivP)]⁻, recorded at the temperatures, applied fields (**B**), and angles between **B** and incident γ -radiation as indicated. The simulations (solid lines) in series A (left) are obtained with the spin-Hamiltonian parameters $D = -0.6\text{ cm}^{-1}$, $E/D = 0$, $A_x = A_y = -15.5\text{ T}$ and, in series B (right), with $D = -0.9\text{ cm}^{-1}$, $E/D = 0.333$, and $A_x = A_y = -17.0\text{ T}$. The other parameters are, in both series, as given in Table I. The relaxation modes, adopted in the simulations, are indicated.

perature (1.5–200 K), are presented in Figure 4, together with spin-Hamiltonian simulations displayed by the solid curves. The weak temperature dependence of the quadrupole splitting indicates

that the ground orbital state is energetically well-isolated, which justifies application of the spin-Hamiltonian formalism in the description of the magnetic properties of the ground spin multiplet. The spin Hamiltonian, $\mathbf{H} = \mathbf{H}_e + \mathbf{H}_n$, is the sum of an electronic part of the form¹⁷

$$\mathbf{H}_e = D[S_z^2 - S(S+1)/3] + E[S_x^2 - S_y^2] + \beta_e \mathbf{B} \cdot \mathbf{g} \cdot \mathbf{S} \quad (1)$$

describing the zero-field splittings and Zeeman interactions between electrons and the applied field, and a nuclear part¹⁷

$$\mathbf{H}_n = \mathbf{H}_Q - g_n \beta_n \mathbf{B} \cdot \mathbf{I} + g_n \beta_n \mathbf{S} \cdot \mathbf{A} \cdot \mathbf{I} + \delta \quad (2)$$

describing the electric quadrupole interaction, Zeeman interaction between the nucleus and the applied field, the magnetic hyperfine interaction of the electrons and the nucleus, and the isomer shift, respectively. Sufficiently large applied fields are used to decouple the electronic secular problem from the nuclear one. The electron-spin operator, \mathbf{S} , in eq 2 can then be replaced by the spin expectation value, $\langle \mathbf{S} \rangle$. In calculating the spin expectation values, the dynamic properties of the electron spin are accounted for in either the slow- or the fast-relaxation limit.¹⁸ In the slow limit, the Mössbauer spectra are Boltzmann-weighted summations over subspectra calculated with internal fields, $\langle \mathbf{S} \rangle_i \mathbf{A}$, generated by the individual electronic eigenstates, $|i\rangle$. In the fast limit, the spectra are the result of an interaction between the nucleus and a single effective field that is the thermal average, $\langle \langle \mathbf{S} \rangle \rangle_T \mathbf{A}$, of the internal fields associated with the electronic eigenstates. The zero-field spectra, mentioned above, show fast-relaxation behavior. The relaxation limits adopted in the simulations of the magnetic spectra are given in Figure 4.

At high temperatures the internal fields average to zero so that the Mössbauer spectra recorded in applied field are determined by the combined effect of the nuclear Zeeman and electric quadrupole interactions. The pattern of the spectrum recorded at 200 K in a field of 6.21 T (Figure 4e) is characteristic for a positive value of the largest component of the electric field gradient and a vanishing value of the asymmetry parameter, η .¹⁹ In all our simulations, the principal axes of the \mathbf{D} , \mathbf{EFG} , \mathbf{A} , and \mathbf{g} tensors are taken parallel. (Our analysis allows of both parallel and perpendicular oriented main principal \mathbf{EFG} and \mathbf{D} tensor axes. The main principal axis of a tensor is defined as the principal axis which corresponds to the eigenvalue with the largest magnitude). The principal \mathbf{A} tensor components, $A_x = A_y$, and A_z , were determined by adjusting the calculated line positions to those observed in the spectra. The zero-field parameter D was obtained from the field dependence of the spectra. In the determination of the rhombicity parameter, E , we considered the two extreme cases, viz., axial symmetry, $E = 0$, and maximal rhombicity, $E = D/3$, resulting in the simulations depicted in series A and B of Figure 4, respectively. The fast-relaxation simulation for $E = 0$ (and $D = -0.6 \text{ cm}^{-1}$) at 1.5 K in 60 mT yields a doublet with too narrow lines (Figure 4a, A), whereas in the slow-relaxation simulation broad bands are obtained instead of the observed doublet pattern. A qualitatively similar behavior is found for $E = D/3$ (and $D = -0.9 \text{ cm}^{-1}$), but with the simulation in slow relaxation (Figure 4a, B) showing better agreement with experiment than for $E = 0$. The spin fluctuations at 1.5 K and 60 mT can apparently only be correctly described in the framework of intermediate-relaxation theory. We note that the variation of the absorption lines between -0.75 and $+1.5 \text{ mm s}^{-1}$ in the high-field spectra, caused by increasing the temperature from 1.5 (Figure 4b) to 4.2 K (Figure 4c), results also from incipient intermediate-relaxation behavior, which develops quickly in the spectra recorded at more elevated temperatures (not shown). Due to the marginal effect of the spin fluctuations in the high-field, low-temperature spectra, the slow-relaxation limit is an acceptable approximation for simulating the experimental hyper-fine patterns

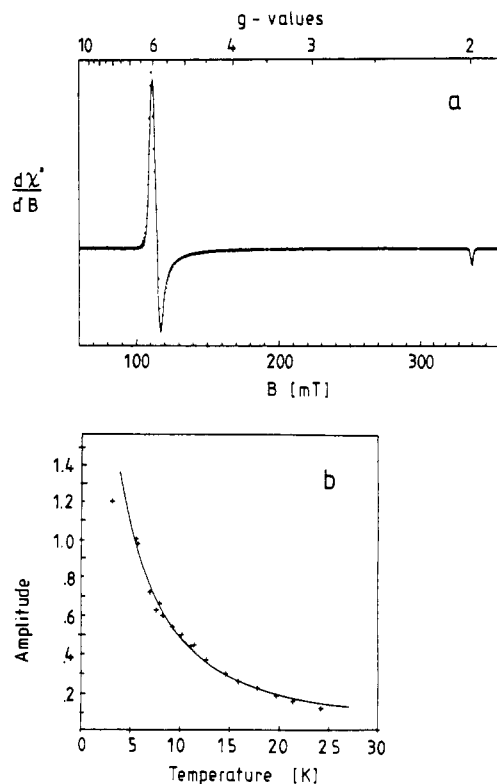


Figure 5. (a) EPR spectrum of the ferric complex $[\text{Fe}^{\text{III}}(\text{CH}_3\text{CO}_2)_2(\text{TPpivP})]$, recorded at 3.31 K. The simulation (solid curve) is based on an effective spin $S' = 1/2$ description of the lowest Kramers doublet, $|^5/2, \pm 1/2\rangle$, with effective g values 5.88, 6.05, and 2.0. (b) Temperature dependence of the doubly-integrated EPR signal, recorded in the ferric complex $[\text{Fe}^{\text{III}}(\text{CH}_3\text{CO}_2)_2(\text{TPpivP})]$. The solid curve represents the theoretical result for the temperature dependence, eq 3, calculated with the zero-field parameter, $D = 7.5 \text{ cm}^{-1}$, obtained by a least-squares fit of the experimental data.

in Figure 4b–d. Where the slow-relaxation limit is appropriate, simulations obtained in the rhombic case (B) show somewhat better agreement with experiment than in the axial case (A). Furthermore, in the low-field, low-temperature spectrum (Figure 4a) the spin-fluctuation behavior is expected to be close to the slow-relaxation limit, since the spin-expectation values, and, thus, spin-dipolar couplings, are small, and the lattice dynamics slow. Therefore, we tentatively conclude that $E/D \approx 1/3$. This value and those for the other spin-Hamiltonian parameters used in the simulations in series B are summarized in Table I.

3.3. EPR and Mössbauer Analysis of the Ferric Complex. Figure 5a depicts the X-band EPR spectrum recorded in a polycrystalline sample of the ferric complex $[\text{Fe}^{\text{III}}(\text{CH}_3\text{CO}_2)_2(\text{TPpivP})]$ and a simulation based on the effective spin $S' = 1/2$ description of the EPR-active Kramers doublet, $|^5/2, \pm 1/2\rangle$. The obtained effective g values, $g^e = 5.88, 6.05$, and 2.0, are characteristic for ferric high-spin iron. The slight anisotropy between the two largest g tensor components, $\Delta g = 48E/D = 0.17$, corresponds with a rhombicity parameter $E = 0.004D$. The zero-field splittings in the ground spin multiplet are thus described by an almost axially symmetric spin Hamiltonian. The temperature dependence of the EPR spectra reveals a low-lying Kramers doublet $|^5/2, \pm 1/2\rangle$ and, thus, a positive D value. The magnitude of the zero-field parameter, $D = 7.5 \text{ cm}^{-1}$, was determined by fitting the approximate expression for the temperature dependence of EPR intensity

$$F = 1/[T(1 + \exp(-2D/kT) + \exp(-6D/kT))] \quad (3)$$

to the doubly-integrated experimental spectra recorded in the temperature range 5–25 K (see Figure 5b). The factor $1/T$ represents the Curie–Weiss behavior of the signal of the EPR-active Kramers doublet $|^5/2, \pm 1/2\rangle$; the exponential terms result from Boltzmann distribution over the three Kramers doublets in the ground spin multiplet.

(17) Abragam, A.; Bleaney, B. *Electron Paramagnetic Resonance of Transition Ions*; Dover Publications: New York, 1986.

(18) Güthlich, P.; Link, R.; Trautwein, A. X. *Mössbauer Spectroscopy and Transition Metal Chemistry*; Springer-Verlag: Berlin, 1978.

(19) Collins, R. L.; Travis, J. C. In *Mössbauer Effect Methodology*; Gruverman, I. J., Ed.; Plenum Press: New York, 1967; Vol. III.

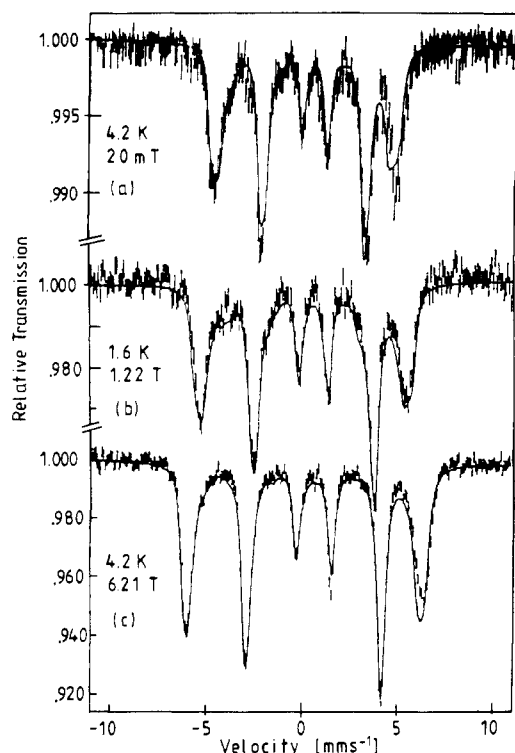


Figure 6. Mössbauer spectra of the ferric complex $[\text{Fe}^{\text{III}}(\text{CH}_3\text{CO}_2)(\text{TPpivP})]$, recorded at the temperatures and fields (B), applied perpendicular to the incident γ -radiation, indicated. The simulations (solid lines) are obtained with the spin-Hamiltonian parameters tabulated in Table V, in slow relaxation.

The zero-field, high-temperature Mössbauer spectra of the ferric species (not shown) exhibit a quadrupole splitting $\Delta E_Q = 1.1 \text{ mm s}^{-1}$ and isomer shift $\delta = 0.4 \text{ mm s}^{-1}$. The magnetic low-temperature spectra, recorded at 1.6–4.2 K in fields of 20 mT to 6.21 T applied perpendicular to the γ -beam, are presented in Figure 6, together with the results of spin-Hamiltonian simulations. Large magnetic hyperfine splittings are already reached in small applied fields of $B \geq 20 \text{ mT}$. The spin expectation values thus saturate in small fields, a property characteristic for Kramers systems. The sign and magnitude of the velocity shift of the two outer absorption lines relative to the inner line quartet in Figure 6, show that the component of the electric field gradient in the direction of the internal field is negative and its magnitude half that of the main component of the EFG tensor deduced from the zero-field spectra. The internal field is predominantly oriented in the xy plane; thus the main component of the EFG tensor, $V_{zz} = -V_{xx} - V_{yy}$, is in the z direction and is positive. The value of the asymmetry parameter is zero. The line positions could be reproduced on the basis of an isotropic magnetic hyperfine tensor, $A_x = A_y = A_z$. We note, however, that the value of A_z is determined with lower accuracy than of A_{xy} , since the spin expectation values are mainly oriented in the xy plane. The low-field, low-temperature spectra originate from the low-energy Kramers doublet $|5/2, \pm 1/2\rangle$, since $kT < D$. The field dependence of the overall magnetic splittings in the low-temperature spectra is a measure for the mixing between the Kramers doublets caused by Zeeman interaction and provides information about the relative magnitudes of the zero-field and Zeeman splittings. The analysis of the field dependence yields a zero-field parameter, $D = 7.5 \text{ cm}^{-1}$, in excellent agreement with the value obtained from the EPR study. The Mössbauer spectra are compatible with the small value for the rhombicity parameter deduced from the EPR analysis. Table V summarizes the spin-Hamiltonian parameters of the ferric species.

4. Interpretation and Discussion

4.1. Ferrous Complex. The present analysis of the Mössbauer data recorded in the ferrous acetate complex $[\text{Fe}^{\text{II}}(\text{CH}_3\text{CO}_2)(\text{TPpivP})]^-$ yields spectral fits of the same quality as those previously reported in ref 9, although being more restrained by using

Table V. Spin $S = 5/2$ Hamiltonian Parameters, Obtained from EPR and Mössbauer Analyses, of the Ferric High-Spin Complex $[\text{Fe}^{\text{III}}(\text{CH}_3\text{CO}_2)(\text{TPpivP})]$

ΔE_Q , mm s^{-1}	+1.1 ^a
η	0 ^b
δ , mm s^{-1}	0.40 ^{a,c}
Γ , mm s^{-1}	0.40
g_x	1.960 ^d
g_y	2.017 ^d
g_z	2
$A_x = A_y = A_z$, T	-20.0
D , cm^{-1}	7.5
E/D	0.004 ^e

^a Measured at 4.2 K. ^b Not varied in the simulations. ^c Relative to α -Fe at room temperature. ^d Calculated from the EPR values for the effective g^z factors by $g_{x,y} = g_{x,y}^z/3$. ^e Value obtained from EPR analysis; it is taken to be zero in the simulations of the Mössbauer spectra.

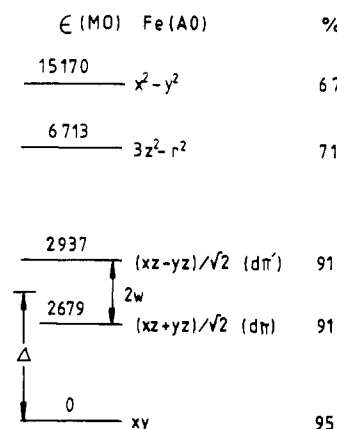


Figure 7. Schematic energy (ϵ) diagram of the molecular orbitals (MO) of predominantly 3d character, computed by MO calculation in the truncated structure of the ferrous complex $[\text{Fe}^{\text{II}}(\text{CH}_3\text{CO}_2)(\text{TPpivP})]^-$, described in the text. Energies are in cm^{-1} . The percentage given at each molecular orbital denotes $c^2 \times 100\%$, with c being the largest linear-combination coefficient occurring in the MO and belonging to the Fe 3d atomic orbital (AO) indicated. The energy parameters are $\Delta = 2808 \text{ cm}^{-1}$ and $w = 129 \text{ cm}^{-1}$.

collinear principal axes for **D**, **EFG**, **A**, and **g** tensors, axially symmetric **A** tensors, and fixed **g** values equal to 2. The values for ΔE_Q , η , δ , and **A** tensor components are almost identical to those reported for the phenolate complex $[\text{Fe}^{\text{II}}(\text{OC}_6\text{H}_5)(\text{TPP})]^-$ (Table I). The zero-field parameter **D** in the acetate complex has only half the value found in the phenolate complex. The discrepancy between the rhombicity parameters in the two complexes (Table I) is a matter of parameter constraint, since the rhombicity parameter **E** was kept equal to zero throughout the analysis of the phenolate complex.⁸

In order to estimate the zero-field splittings in the complex $[\text{Fe}^{\text{II}}(\text{CH}_3\text{CO}_2)(\text{TPpivP})]^-$ theoretically, we first solve the electrostatic problem in the molecular-orbital approximation. The molecular orbitals were calculated by means of the iterative self-consistent-charge linear-combination-of-atomic-orbital procedure described elsewhere.²⁰ The molecular framework adopted in the calculations is the X-ray structure, truncated, for computational convenience, by replacing the pivalamide pickets by hydrogen atoms. The resulting energies of the molecular orbitals of predominant iron 3d character are presented in Figure 7. The number given next to each 3d orbital indicates the percentage of its weight in the corresponding molecular orbital; the complement of this number to 100% represents orbital delocalization toward the ligands plus a slight intra-3d-shell mixture. The xy character of the doubly-occupied, low-energy 3d orbital found in the calculation confirms the oblate character of the orbital ground state inferred from the electric- and magnetic-hyperfine interactions.^{8,9}

(20) Grodzicki, M.; Manning, V.; Trautwein, A. X.; Friedt, J. M. *J. Phys. B* 1987, 20, 5595.

Furthermore, the energy gap of $\geq 2679 \text{ cm}^{-1}$ between the ground and excited orbital states is in accordance with the weak temperature dependence of the quadrupole splitting. The mixture between the two $d\pi$ orbitals is related to the orientation of the OCO^- moiety in the acetate ligand along the bisector of the x and y axes (see Figure 2).

The zero-field tensor, \mathbf{D} , occurring in the zero-field operator, $\sum \mathbf{D}_{pq} \mathbf{S}_p \mathbf{S}_q$, is calculated by substitution of the energies and the Fe 3d parts of the molecular orbitals indicated in Figure 7 into the second-order perturbation expression¹⁷

$$\mathbf{D}_{pq} = -\lambda^2 \sum \frac{\langle 0 | \mathbf{L}_p | n \rangle \langle n | \mathbf{L}_q | 0 \rangle}{\epsilon(n) - \epsilon(0)} \quad (4)$$

with \mathbf{L}_p denoting the component $p = x, y, \text{ or } z$ of the orbital-momentum operator of the iron ion, $\lambda = -100 \text{ cm}^{-1}$ denoting the spin-orbit coupling constant in $\lambda \mathbf{L} \cdot \mathbf{S}$, $\epsilon(n)$ denoting the energy of the electronic state $|n\rangle$ with the excess electron occupying the 3d-type orbital n , and the summation being over n , excluding the ground configuration. The zero-field splitting is a second-order effect, which can be classically visualized as resulting from the circular currents generated in the atomic shell by the electron spin. These currents produce magnetic fields which in turn tend to orient the spin. In the numerical application of expression 4, the energies $\epsilon(n)$ are identified with the corresponding molecular-orbital energies calculated in the ground configuration (see Figure 7). After transformation of tensor \mathbf{D} to principal axes and subtraction of the trace, \mathbf{D} takes the diagonal form, (d_x, d_y, d_z) with $d_x + d_y + d_z = 0$. The zero-field operator can then be expressed as $\mathbf{H}_{zf} = D[S_z^2 - S(S+1)/3] + E[S_x^2 - S_y^2]$ with $D = -(d_x + d_y - 2d_z)/2$ and $E = (d_x - d_y)/2$. The labels X, Y, Z are the permutation of X', Y', Z' for which the inequalities $|d_z| \geq |d_y| \geq |d_x|$ and $0 \leq E_z/D_z \leq 1/3$ hold. Subsequently, we calculated the EFG tensor, \mathbf{V} , by means of the expression¹⁷

$$\mathbf{V}_{pq} = q' [\langle 0 | (\mathbf{L}_p \mathbf{L}_q + \mathbf{L}_q \mathbf{L}_p) / 2 | 0 \rangle - 2\delta_{p,q}] \quad (5)$$

with $q' = e^2 Q \langle r^{-3} \rangle / 21$, $Q = 0.17$ barn, denoting the nuclear quadrupole moment of ^{57}Fe ,²¹ and $\langle r^{-3} \rangle = 5 \text{ bohr}^{-3}$, which is the radial average of r^{-3} over the 3d orbitals. We notice that the EFG is, according to eq 5, a property of the orbital ground state, whereas the zero-field tensor (eq 4) depends on the ground as well as excited orbital states and energies. After transformation of \mathbf{V} to principal axes, we evaluated the angle, β , between the "main" principal axes of the \mathbf{D} and EFG tensors. (The "main" principal axes are defined as the axes corresponding to the eigenvalues of largest magnitudes). The calculation for the ferrous acetate porphyrinate complex results in the zero-field parameters $D = -2.6 \text{ cm}^{-1}$, $E/D = 0.11$, quadrupole splitting $\Delta E_Q = +3.9 \text{ mm s}^{-1}$, and angle $\beta = 85^\circ$. The sign and order of magnitude of the calculated value for D agree with spin-Hamiltonian parameters deduced from experiment, but the almost orthogonal orientation of the main principal axes of the \mathbf{D} and EFG tensors conflicts with the parallel alignment adopted in the analysis of the Mössbauer data.

In order to understand the discrepancy between the theoretical and experimental results for the zero-field parameters, we analyze the dependence of these parameters on the electronic structure of the 3d shell in the iron(II) ion. We adopt at first pure 3d orbitals in the description of the iron ion. The t_{2g} ground triplet of the iron ion is split by distortions from octahedral symmetry in orbitals of the form xy , $d\pi$, and $d\pi'$, with $d\pi = (\cos \theta)(xz) + (\sin \theta)(yz)$ and $d\pi' = (\sin \theta)(xz) - (\cos \theta)(yz)$ (this rotation in orbital space gives rise to a similar rotation of the principal axes of the \mathbf{D} tensor). When the summation in expression 4 is restricted to the lowest 3d-orbital triplet, the zero-field parameters become a function of the energy parameters Δ and w , indicated in Figure 7. In the case where the energy gap between the two lower levels is greater than or equal to the separation between the upper pair ($w/\Delta \leq 1/3$) the zero-field parameters are $D = \lambda^2 \Delta / (\Delta^2 - w^2)$

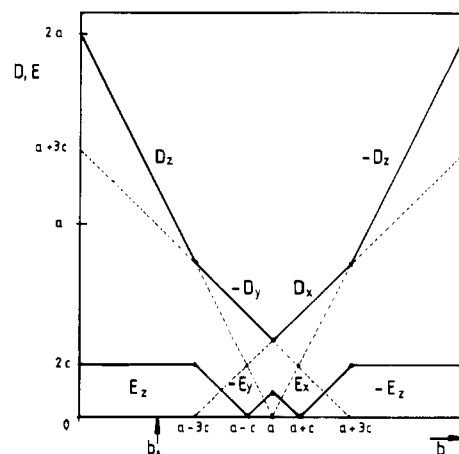


Figure 8. Schematic representation of the dependence of the zero-field parameters D_p and E_p , $0 \leq E_p/D_p \leq 1/3$, (bold lines) in a high-spin Fe(II) complex with a low-energy xy orbital, as a function of the parameter $b = 2\lambda^2/\epsilon(x^2 - y^2)$, based on the idealized energy diagram 0 ($\epsilon(xy)$), $\Delta - w$ ($\epsilon(yz)$), $\Delta + w$ ($\epsilon(xz)$), and $\epsilon(x^2 - y^2)$, (see Figure 7). The subscript $p = x, y, \text{ or } z$ indicates the direction of the main principal axis of the \mathbf{D} tensor relative to the 3d-orbital frame. The parameters a and c are defined as $a = \Delta\lambda^2/(2(\Delta^2 - w^2))$ and $c = w\lambda^2/(2(\Delta^2 - w^2))$. The quotient E_p/D_p reaches its maximal value, $1/3$, at the values $a - 3c$, a , and $a + 3c$. The energies are expressed in arbitrary units.

and $E = (w/\Delta)D$. D is then positive, and the main principal axis of the \mathbf{D} tensor is oriented perpendicular to the xy plane. This can be regarded as the effect of circular currents around the x and y axes, which arise from admixing the $|xz\rangle$ and $|yz\rangle$ orbital into the $|xy\rangle$ ground state. The resulting magnetic fields point perpendicular to the z axis and favor thus energetically the $S_z = 0$ substate as it is described by a positive D . If, however, one of the currents is much larger than the other, one has to take the corresponding field direction, x or y , as the new quantization axis. With respect to it, now $|S_z| = 2$ is stabilized. This is the case when the energy gap between the upper two levels exceeds the separation between the lower pair ($w/\Delta > 1/3$), yielding for the zero-field parameters $D = -\lambda^2(\Delta + 3w)/(2(\Delta^2 - w^2))$ and $E = ((\Delta - w)/(\Delta + 3w))D$. D is indeed negative, and the main axis of the \mathbf{D} tensor is oriented along the xy plane. As the excess electron occupies the xy orbital, the main axis of the EFG tensor is oriented perpendicular to the xy plane, i.e., either parallel ($w/\Delta \leq 1/3$) or perpendicular ($w/\Delta > 1/3$) to the main axis of the \mathbf{D} tensor. However, neither of the two cases conforms with the conjunction of negative D and parallel main \mathbf{D} and EFG tensor axes deduced from experiment. Furthermore, the value $w/\Delta = 0.05$ ($\leq 1/3$) obtained from the molecular-orbital calculations implies, in the framework of the "three-orbital" model, a positive D value, in disagreement with the value $D = -2.6 \text{ cm}^{-1}$ evaluated by summing over the complete 3d-orbital space in expression 4. Therefore, we now proceed by analyzing the effect of the $|x^2 - y^2\rangle$ and $|3z^2 - r^2\rangle$ states on the zero-field splitting, neglecting any admixture between the 3d basis orbitals due to an off-diagonal ligand-field interaction.

The dependence of the zero-field parameters D and E ($0 \leq E/D \leq 1/3$) and of the orientation of the corresponding main principal axes relative to the 3d-orbital frame on the energy parameter $b = 2\lambda^2/\epsilon(x^2 - y^2)$ is depicted in Figure 8, for the case $w/\Delta \leq 1/3$. We note that the electronic state $|3z^2 - r^2\rangle$ does not interact with the orbital ground state, $|xy\rangle$, by spin-orbit coupling and, therefore, does not affect the zero-field splitting. For an infinitely large value of $\epsilon(x^2 - y^2)$ ($b = 0$), the rhombicity parameter takes the value $E = (w/\Delta)D$, as in the three-orbital model. For decreasing $\epsilon(x^2 - y^2)$ (i.e. increasing b), the zero-field parameter D appears in the order $D_z \geq 0$, $D_y \leq 0$, $D_x \geq 0$, $D_z \leq 0$, which could be made plausible in the classical picture of circular currents, too. Due to the intrusion of the $|x^2 - y^2\rangle$ state, the zero-field parameters D can also assume the values $D_z < 0$ and $D_\perp > 0$ ($\perp = x \text{ or } y$), next to the values $D_z \geq 0$ and $D_\perp \leq 0$ arising in the three-orbital model. The values of b at which the rhombicity is

(21) Bominaar, E. L.; Guillin, J.; Sawaryn, A.; Trautwein, A. X. *Phys. Rev. B* 1989, 39, 72.

a maximum, i.e., $b = a - 3c$, $b = a$, and $b = a + 3c$ indicated on the abscissa in Figure 8, pertain, after substitution of the computational results for w and Δ in the expressions $a = \lambda^2/(2(\Delta^2 - w^2))$ and $c = \lambda^2 w/(2(\Delta^2 - w^2))$, to the orbital energies $\epsilon(x^2 - y^2) = 1.3 \times 10^4$, 1.1×10^4 , and 0.99×10^4 cm⁻¹, respectively. The zero-field parameters, $D_z = -0.9$ cm⁻¹ and $E/D = 1/3$, obtained from the spin-Hamiltonian analysis of the Mössbauer data in the ferrous complex, can be assigned to $b = a + 3c$ in Figure 8. Changes in the state energy $\epsilon(x^2 - y^2)$ of only about 500 cm⁻¹ in the intervals $(a, a + c)$, $(a, a - c)$ and of 1000 cm⁻¹ in the intervals $(a + c, a + 3c)$, $(a - c, a - 3c)$ lead to E values covering the complete range of rhombicity, $E/D = 0$ to $1/3$. Also changes in the energy gap $2w$ between the two $d\pi$ levels have a considerable impact on the zero-field parameters. The reduction of $2w$ from the calculated value 258 cm⁻¹ ($c \neq 0$) to zero ($c = 0$) leads to the coincidence of the values $a - 3c$ and $a + 3c$ on the abscissa in Figure 8, and makes the rhombicity parameter vanish for all values of b . A strong dependence of the zero-field parameters on the energies $\epsilon(x^2 - y^2)$, $\epsilon(d\pi)$, and $\epsilon(d\pi')$ gives rise to considerable couplings of the electron spin to nuclear-vibration modes that affect these energies and may cause the dynamics in the Mössbauer spectra. Stacking-induced variations of the rhombicity parameter possibly underlie the difficulties encountered in the determination of the value of E in the acetate complex.

We note that the out-of-plane shift of the iron ion reduces the antibonding interaction between the $x^2 - y^2$ electron and the pyrrole nitrogen atoms, which leads to a reduction of the admixture of the ligand orbitals into the $x^2 - y^2$ -type molecular orbital, to lowering of the energy $\epsilon(x^2 - y^2)$, and to larger values for parameter b .

Thus far, we have disregarded linear combination among 3d orbitals caused by low-symmetry components in the ligand field. Although the intra-3d-shell admixture coefficients obtained in the molecular-orbital calculation, apart from those occurring in the $d\pi$ -type orbitals, are small ($|\delta_e| \leq 0.1$), their effect on the zero-field splittings is considerable. Complete neglect of intra-3d-shell mixing in the evaluation of the D tensor using eq 4 results in a positive zero-field parameter $D_z = 1.4$ cm⁻¹ (corresponding to, e.g., b_A in Figure 8), whereas a negative value, $D_y = -2.6$ cm⁻¹, is obtained if the admixtures are accounted for. A detailed analysis shows that the change in the sign of D is generated by the admixture of the $3z^2 - r^2$ orbital into the ground orbital, $xy + \delta_e(3z^2 - r^2)$, irrespective of other admixtures. The effect of this admixture on the zero-field splittings can be mimicked by adopting $w = 2\delta_e\Delta\sqrt{3}$ in our crystal-field analysis, provided that $|\delta_e| \ll 1$ and $\Delta = \epsilon(xz) = \epsilon(yz)$. The value for $a - 3c$ is then shifted by the admixture to the left of b_A on the abscissa in Figure 8, leading to negative D and $\beta = 90^\circ$ ($D_y < 0$) at b_A . The values of the zero-field parameters are thus found to depend sensitively on the energies and the linear-combination coefficients of the molecular orbitals. It is, therefore, expected that methodological details in the computational scheme have a considerable impact on the values of calculated zero-field parameters.

In order to analyze the relation between the X-ray structure and the zero-field splittings in the ferrous complex, the parameters D , E , and β are also calculated in both the symmetrized and the distorted structures indicated in Figure 3, again by combining expressions 4 and 5. In order to avoid the intricacies inherent to molecular-orbital calculations, we adopt for this purpose a crystal-field model in which the iron-ligand interactions are mimicked by five point charges at the corresponding positions in the first ligand shell of the iron ion, plus four point charges, B, at the bisectors of the x and y axes at fixed distances of 1.1 Å from Ct, that serve to impose the correct energy order in the low-energy orbital triplet, i.e., $\epsilon(xy) < \epsilon(xz, yz)$. The radial dependence of the 3d orbitals, which are the only orbitals considered in these calculations, is taken from the standard Fe(5D) basis set given by Huzinaga.²² The point charges, q , adopted

Table VI. Zero-Field Parameters and Angle, β , between the Main Principal Axes of the D and EFG Tensors, Obtained by Combining Eqs 4 and 5, on the Basis of the Crystal-Field Solutions for the 3d Orbitals and Their Energies, Calculated in the Symmetrized, Distorted (a, ..., e), and X-ray (a + ... + e) Structures Presented in Figure 3

structure	D , cm ⁻¹	E/D	β , deg
symmetrized	+1.1	0.00	0
a	+1.9	0.20	38
b	+1.9	0.14	38
c	+1.1	0.06	0
d	+1.4	0.15	24
e	-1.7	0.14	83
a + b + c + d + e	+2.0	0.23	44

in the calculations, are $q(B) = 0.66$ e, $q(O_{\text{acetate}}) = -7.86$ e, and $q(N_p) = -8.52$ e, and give rise, in the symmetrized conformation, to relative orbital energies of 0 cm⁻¹ (xy), 2921 cm⁻¹ (xz, yz), 6778 cm⁻¹ ($3z^2 - r^2$), and 17544 cm⁻¹ ($x^2 - y^2$), close to the molecular orbital energies given in Figure 7. The results of the calculations are summarized in Table VI. The zero-field parameter in the symmetrized structure is like that evaluated before on the basis of the molecular-orbital procedure after neglect of the intra-3d-shell mixtures ($D_z > 0$, $\beta = 0^\circ$; b_A in Figure 8). The admixture coefficient δ_e of the $3z^2 - r^2$ orbital into the ground orbital, xy , is in magnitude less than 0.04 for all structures considered; the largest value of δ_e is found for the distortion (e), leading to $D_\perp < 0$. The distortions of the Fe (b) and O_{acetate} (a) positions in the complex give rise to almost a doubling of the D value in the symmetrized structure and angles of 38°.

The intermediate value of the angle $\beta = 44^\circ$ obtained with the point-charge model in the X-ray structure, (a + ... + e), is not reproduced by the molecular-orbital calculation, which indicates that the two methods possess different orbital-mixing abilities. The discrepancy in the computational results document the need for further advancement of computational procedures for evaluating fine-structure data.

4.2. Ferric Complex. The values of the hyperfine parameters in the ferric high-spin $S = 5/2$ complex $[\text{Fe}^{\text{III}}(\text{CH}_3\text{CO}_2)(\text{TPPivP})]$, tabulated in Table V, are as usually found in ferric high-spin porphyrins. The nonvanishing quadrupole splitting, $\Delta E_Q = 1.1$ mm s⁻¹, monitors an aspherical charge distribution around the iron nucleus. The positive sign of the main component of the EFG tensor indicates an excess of electron charge in the iron-porphyrin plane. The asymmetry in the charge distribution has to originate entirely from the presence of the ligands, since the high-spin ground state of unperturbed iron(III) has a spherically symmetric, half-filled 3d-shell configuration, 6S . We note in passing that the partitioning of the quadrupole splitting in the ferrous complex into Fe 3d-shell and ligand contributions entails a value of $(4.25 - 1.1)$ mm s⁻¹ = 3.15 mm s⁻¹ for the 3d part.

The isotropy of the A tensor reveals an internal field originating from Fermi contact interaction.¹⁷ The dipolar term is found to be zero, in contrast to that in the ferrous complex. The spin density in the ferric complex is, in the spin-Hamiltonian analysis of the magnetic hyperfine interaction, not discernible from the spherical distribution present in unperturbed 6S ions.

The zero-field parameter $D = 7.5$ cm⁻¹ in the ferric complex lies within the range of D values observed in other five-coordinate ferric high-spin porphyrins ($4 \leq D \leq 20$ cm⁻¹).^{23,24} Within the ground LS term, 6S , of the iron(III) ion, denoted by 6A_1 in O_h and C_{4v} symmetry, the matrix elements of the spin-orbit coupling operator vanish. For this reason, the zero-field splittings in the ground spin multiplets of ferric high-spin complexes are, in contrast to those in ferrous high-spin species, generally assumed to originate from spin-orbit interaction of the atomic ground LS term with excited LS terms of spin $3/2$. A detailed analysis shows that the zero-field splittings in ferric high-spin porphyrins originate mainly

(22) Huzinaga, S.; Andzelm, J.; Klobukowski, M.; Radzio-Andzelm, E.; Sakai, Y.; Tatewaki, H. *Gaussian Basis Sets for Molecular Calculations*; Elsevier: Amsterdam, 1984.

(23) Scheidt, W. R.; Gouterman, M. In *Iron Porphyrins*; Lever, A. B. P., Gray, H., Eds.; Addison-Wesley Publ. Co.: London, 1983; Part I.
(24) Loew, G. In *Iron Porphyrins*; Lever, A. B. P., Gray, H., Eds.; Addison-Wesley Publ. Co.: London, 1983; Part I.

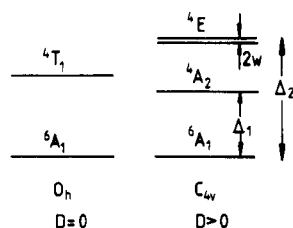


Figure 9. Scheme of electronic terms contributing to the zero-field splittings in high-spin iron(III) porphyrins, according to a model proposed by Griffith.²⁵

from the interaction of the ground term 6A_1 with a low-lying 4A_2 term (C_{4v} symmetry), which splits off from a 4T_1 term in O_h symmetry by weakening of the axial component in the ligand field, as indicated in Figure 9.²⁵ In octahedrally coordinated ions, the zero-field parameters D and E are identically zero for symmetry reasons. The spin-quartet term is then, in first-order approximation, found to be uniformly admixed into the three Kramers doublets, $M_s = \pm 1/2, \pm 3/2$, and $\pm 5/2$, of the ground spin multiplet. In axial symmetry, however, the energy separation between the 4A_2 and the 4E terms causes a nonuniform admixture of spin-quartet states into the three ground-state doublets, which leads to nonvanishing values for the zero-field parameters. The expression for the zero-field parameter D , obtained by treating the one-electron spin-orbit interaction, $\zeta \sum l_i s_i$, of 6A_1 with the 4A_2 and 4E terms in second-order perturbation theory, reads²⁵

$$D = (\zeta^2/5)(1/\Delta_1 - 1/\Delta_2) \quad (6)$$

The positive sign of D , found in the present work and all other ferric high-spin porphyrins, confirms, according to eq 6, the increasing energy order of the 4A_2 and 4E terms, inferred from crystal-field theory.²⁵

The average of the two perpendicular components of the effective g tensor, $g_{\perp}^e = (g_x^e + g_y^e)/2$, in the ferric species is slightly reduced ($g_{\perp}^e = 5.965$) relative to the high-spin value, $g_{\perp}^e = 6$, due to admixture of spin quartet states with $g_{\perp}^e = 4$. The expressions for the effective g values, derived from first-order wave functions in axial symmetry, read

$$g_{\perp}^e = 6 - (12\zeta^2/5)(1/\Delta_1^2 + 1/\Delta_2^2) \quad (7a)$$

$$g_{\parallel}^e = 2 - 8\zeta^2/5\Delta_2^2 \quad (7b)$$

By combining eqs 6 and 7a with the values for $D = 7.5 \text{ cm}^{-1}$ and $g_{\perp}^e = 5.965$ in the ferric complex, we can resolve the parameters Δ_1 and ζ in dependence on Δ_2 . If the 4E term is disregarded ($\Delta_2 = \infty$), the solutions are $\zeta = 311 \text{ cm}^{-1}$ and $\Delta_1 = 2571 \text{ cm}^{-1}$. For finite but large values of Δ_2 ($\gg \Delta_1$), we may neglect, in good approximation, the quadratic terms $(\zeta/\Delta_2)^2$ in expression 7. In this approximation, the effective g values depend only on the interaction of 6A_1 with the 4A_2 term, whereas the zero-field parameter D is determined by the interactions with both the 4A_2 and 4E terms. In order to match the experimental datum of D in the case $\Delta_2 < \infty$, the coupling constant ζ has to assume values larger than 311 cm^{-1} to compensate for the negative contribution to D due to the 4E term. The range of allowed ζ values, $\zeta > 311 \text{ cm}^{-1}$, contains the spin-orbit coupling constant, $\zeta \approx 400 \text{ cm}^{-1}$, of the free iron(III) ion.¹⁷

Energy splittings ($2w$) between the components of the 4E term (see Figure 9), caused by non-axially-symmetric components in the ligand field experienced by the iron ion, give, in second-order perturbation theory and for $(w/\Delta_2)^2 \ll 1$, rise to a rhombicity parameter

$$E = (w\Delta_1/\Delta_2(\Delta_2 - \Delta_1))D \quad (8)$$

Adopting the experimental values $D = 7.5 \text{ cm}^{-1}$, $E = 0.03 \text{ cm}^{-1}$, $g_{\perp}^e = 5.965$, and $\zeta = 400 \text{ cm}^{-1}$ and resolving eqs 6, 7a, and 8 yield

energy gaps $\Delta_1 = 3312 \text{ cm}^{-1}$, $\Delta_2 = 14809 \text{ cm}^{-1}$, and $2w = 411 \text{ cm}^{-1}$. For these energy-parameter values, the contributions to D , g_{\perp}^e , and g_{\parallel}^e originating from the interaction of 6A_1 with the 4E term are -2 cm^{-1} , 2×10^{-3} , and 10^{-3} , respectively, according to expressions 6, 7a, and 7b. The g^e values are indeed hardly affected by the 4E term. At smaller ζ values ($< 400 \text{ cm}^{-1}$) the solutions for Δ_1 and Δ_2 are reduced and enhanced, respectively, so that the energy splitting between the 4E and 4A_2 terms, $\Delta_2 - \Delta_1$, increases. This energy splitting can be expressed in terms of orbital energies as

$$\Delta_2 - \Delta_1 = 3(\epsilon(x^2 - y^2) - \epsilon(3z^2 - r^2))/4 + \epsilon(xz) - \epsilon(xy) \quad (9)$$

provided that $\epsilon(xz) = \epsilon(yz)$ and rearrangement effects on electron-term energies are negligible. Substitution of the orbital energies calculated in the ferrous complex, given in Figure 7, into eq 9 results in an energy gap, 9150 cm^{-1} , of the same order of magnitude as the value 11497 cm^{-1} deduced from the experimental fine-interaction parameters in the ferric complex using expressions 6–8. The energy splitting, $2w = 411 \text{ cm}^{-1}$, of the 4E term in the ferric complex can be identified with the energy splitting between the two $d\pi$ -orbital levels, and is somewhat larger than the value $2w = 258 \text{ cm}^{-1}$ calculated for the ferrous complex.

5. Conclusion

The Mössbauer investigation of the ferrous form of the acetato-porphyrinato complex reveals a large positive quadrupole splitting ($\Delta E_Q = +4.25 \text{ mm s}^{-1}$). The spin-Hamiltonian analysis of the Mössbauer spectra, adopting collinear principal axes for the EFG, D , A , and g tensors yields a small negative value for the zero-field parameter D (-0.9 cm^{-1}), which is close to the D value (-1.6 cm^{-1}) previously reported in a similar analysis of a related phenolato-porphyrinato complex. Molecular-orbital calculation on the X-ray structure of the ferrous complex reveals a doubly-occupied low-energy $3d$ orbital of xy character and yields a quadrupole splitting of correct sign and magnitude. The theoretical analysis of the zero-field splittings in the ferrous complex shows that the three-orbital model, which considers the spin-orbit interaction between the configurations in which the excess electron of the $3d^6$ configuration of the iron(II) ion is occupying the t_{2g} orbitals, is incomplete: the spin-orbit interaction of the ground configuration with the configuration in which the excess electron is occupying the $x^2 - y^2$ orbital contributes essentially to the zero-field splitting. Relatively small changes in $x^2 - y^2$ -orbital energy may cause drastic changes in the rhombicity parameter E , reorientations of the main principal axis of the D tensor and changes in the sign of the zero-field parameter D . The minute alterations of the wave functions caused by the small deviations from axial symmetry in the ligand shell of the iron(II) ion have a considerable impact on the zero-field parameters. The sensitivity of the zero-field parameters to level energies and wave functions makes the computational results for these parameters rather susceptible to methodological details in the computational schemes adopted. For example, the value of the angle between the main principal axes of the EFG and D tensors calculated in the crystal-field approximation is intermediate ($\beta \approx 44^\circ$) in contrast to the nearly perpendicular orientation obtained from molecular orbital calculation. Reliable predictions of the zero-field parameters in ferrous iron porphyrins seem yet not to be feasible.

The values of the quadrupole splitting, zero-field parameters, and effective g values of the ferric form of the acetato-porphyrinato complex, obtained from Mössbauer and EPR investigations, are as usually found in high-spin iron(III) porphyrins. The rhombicity parameter E has a small but nonvanishing value. The interpretation of the values for the zero-field parameters and the effective g values on the basis of a quantum-mechanical spin admixture of excited 4A_2 and 4E terms into the 6A_1 ground terms due to spin-orbit coupling yields energy differences of about 3000 and 15000 cm^{-1} between the ground and the two excited terms, respectively. The spin-orbit interaction between the ground term and the 4E term has only an insignificant effect on the effective g values ($\Delta g \sim 10^{-3}$), whereas its contribution to the zero-field splitting, although minor, is not negligible ($\Delta D \approx -2 \text{ cm}^{-1}$). The

(25) Griffith, J. S. *The Theory of Transition Metal Ions*; Cambridge University Press: Cambridge, England, 1961.

energy splitting of the 4E term deduced from the experimental datum for the rhombicity parameter E matches roughly the value of the corresponding orbital-level splitting calculated for the ferrous complex.

Acknowledgment. This work was supported by the Deutsche Forschungsgemeinschaft and the Centre National de la Recherche Scientifique (URA 424). R.W. thanks the Alexander von Humboldt Foundation for financial support.

Supplementary Material Available: Table S1, giving thermal parameters of anisotropic atoms, Table S2, giving hydrogen atom positional and thermal equivalent parameters, Table S3, giving a complete set of bond distances, Table S4, giving a complete set of bond angles, Table S6, giving positional parameters and their esd's for $[\text{NaC}222]^+$ and the $\text{C}_6\text{H}_5\text{Cl}$ solvate molecule, and Figure S1, showing a stereoview of the packing in the crystals of $[\text{Fe}(\text{CH}_3\text{CO}_2)\text{TPPivP}][\text{NaC}222]^+\cdot\text{C}_6\text{H}_5\text{Cl}$ (20 pages); Table S5, giving observed and calculated structure factor amplitudes ($\times 10$) for all observed reflections (28 pages). Ordering information is given on any current masthead page.

Contribution from the Institut für Anorganische Chemie, Universität Regensburg, Universitätsstrasse 31, W-8400 Regensburg, Germany, and Department of Chemistry, University of Texas, Austin, Texas 78712-1167

Spectroscopic Studies of Zinc Benzenethiolate Complexes: Electron Transfer to Methyl Viologen

Thomas Türk,[†] Ute Resch,[‡] Marye Anne Fox,^{*,‡} and Arnd Vogler^{*,†}

Received August 12, 1991

Mononuclear and tetranuclear zinc benzenethiolate complexes are studied by both spectroscopic and electrochemical methods. $\text{Zn}(\text{SPh})_4^{2-}$ and $\text{Zn}_4(\text{SPh})_{10}^{2-}$ represent tetrahedral fragments of the cubic zinc sulfide lattice. The structured absorption spectra of the zinc benzenethiolate complexes are ascribed to intraligand transitions for the mononuclear complex and to a composite of both intraligand and ligand-to-metal charge-transfer (LMCT) transitions for the tetranuclear species. The mononuclear complex does not emit, while the tetranuclear compound displays a short-lived metal-to-ligand charge-transfer (MLCT) emission. Photodegradation of both zinc complexes yields thianthrene, dibenzothiophene, and benzenethiol. $\text{Zn}_4(\text{SPh})_{10}^{2-}$ forms a ground-state charge-transfer complex with the dicationic electron acceptor methyl viologen in CH_3CN . Excitation of the charge-transfer absorption band with a 30-ps laser pulse leads to the formation of the methyl viologen radical cation showing a lifetime of 2 ± 0.4 ns.

Introduction

The chemistry of group IIb metal thiolate coordination is vital to an understanding of the interactions of these metals in biological systems.¹ Zinc and cadmium thiolate complexes² have been used as models for thiolate metalloproteins such as metallothioneins,³ which are located in the kidney and liver in a wide variety of animals, including man. These proteins bind various metallic cations such as zinc, cadmium, mercury, and copper through thiolate ligands and regulate the levels of these heavy metals in the organism.⁴

Native metallothioneins³ usually contain six or seven zinc or cadmium atoms bound to all 20 cysteine residues (via mercaptide linkages) in a single polypeptide chain of 61 total amino acid residues.⁴ Each zinc or cadmium atom is coordinated by four cysteine thiolate ligands as deduced from ^{113}Cd NMR studies.⁵ Spectroscopic studies of $\text{Co}(\text{II})$ -⁶ and $\text{Ni}(\text{II})$ -substituted⁷ metallothioneins also indicate tetrahedral $\text{M}(\text{Cys-S})_4$ sites. This tetrahedral coordination requires at least some bridging of the metal ions by cysteine sulfur and suggests that metal-cysteine adamantane-type complexes may be formed in these proteins.^{2b,5d}

Furthermore, short chelating peptides containing cysteine units have been used to synthesize near monodisperse nanometer-scale II-VI semiconductor crystallites⁸ exhibiting size-dependent and discrete excited electronic states that occur at energies higher than the band gap of the corresponding bulk semiconductor.⁹⁻¹² Semiconductor crystallites in the nanometer range (which still show the same crystal structure as the bulk material but are too small to have continuous energy bands) are currently under intense investigation in order to observe the photophysical properties of particles in the quantum-size region (size quantization effect).⁹⁻¹² A further reduction of the particle size yields molecular dimensions exhibiting typical properties such as structured absorption and emission spectra as well as structural rearrangements in the excited state.

In this paper, we report a detailed study of the photophysical and electrochemical behavior of a mononuclear ($\text{Zn}(\text{SPh})_4^{2-}$) and a tetranuclear ($\text{Zn}_4(\text{SPh})_{10}^{2-}$) zinc benzenethiolate complex. The synthesis and crystal structures of these zinc benzenethiolate complexes have been previously described.¹³⁻¹⁵ These tetrahedral

- (1) (a) Carty, A. J. *ACS Symp. Ser.* **1978**, *82*, 327-353.
- (2) (a) Swenson, D.; Baenziger, N. C.; Coucouvanis, D. J. *Am. Chem. Soc.* **1978**, *100*, 1932-1934. (b) Dance, I. G. *J. Am. Chem. Soc.* **1980**, *102*, 3445-3451. (c) Hagen, K. S.; Stephan, D. W.; Holm, R. H. *Inorg. Chem.* **1982**, *21*, 3928-3936. (d) Lacelle, S.; Stevens, W. C.; Kurtz, D. M.; Richardson, J. W.; Jacobson, R. A. *Inorg. Chem.* **1984**, *23*, 930-935. (e) Dance, I. G. *Inorg. Chim. Acta* **1985**, *108*, 227-230. (f) Dance, I. G. *Aust. J. Chem.* **1985**, *38*, 1745-1755.
- (3) Kaegi, J. H. R.; Nordberg, M., Eds. *Metallothionein*; Birkhauser Verlag: Basel, Switzerland, 1979; pp 41-122.
- (4) (a) Kaegi, J. H. R.; Himmelhoch, S. R.; Whanger, P. D.; Bethune, J. L.; Vallee, B. L. *J. Biol. Chem.* **1974**, *249*, 3537-3542. (b) Kojima, Y.; Berger, C.; Vallee, B. L.; Kaegi, J. H. R. *Proc. Natl. Acad. Sci. U.S.A.* **1976**, *73*, 3413-3417.
- (5) (a) Otvos, J. D.; Armitage, I. M. *J. Am. Chem. Soc.* **1979**, *101*, 7734-7736. (b) Otvos, J. D.; Armitage, I. M. *Proc. Natl. Acad. Sci. U.S.A.* **1980**, *77*, 7094-7098. (c) Otvos, J. D.; Olafson, R. W.; Armitage, I. M. *J. Biol. Chem.* **1982**, *257*, 2427-2431. (d) Boulanger, Y.; Goodman, C. M.; Forte, C. P.; Fesik, S. W.; Armitage, I. M. *Proc. Natl. Acad. Sci. U.S.A.* **1983**, *80*, 1501-1505.
- (6) (a) Vasak, M. *J. Am. Chem. Soc.* **1980**, *102*, 3953-3955. (b) Vasak, M.; Kaegi, J. H. R. *Proc. Natl. Acad. Sci. U.S.A.* **1981**, *78*, 6709-6713.
- (7) Vasak, M.; Kaegi, J. H. R.; Holmquist, B.; Vallee, B. L. *Biochemistry* **1981**, *20*, 6659-6664.
- (8) Dameron, C. T.; Reese, R. N.; Mehra, R. K.; Kortan, A. R.; Carroll, P. J.; Steigerwald, M. L.; Brus, L. E.; Winge, D. R. *Nature* **1989**, *338*, 596-597.
- (9) (a) Henglein, A. *Top. Curr. Chem.* **1988**, *143*, 113-180. (b) Henglein, A. *Chem. Rev.* **1989**, *89*, 1861-1873.
- (10) (a) Brus, L. E. *J. Phys. Chem.* **1986**, *90*, 2555-2560. (b) Steigerwald, M. L.; Brus, L. E. *Acc. Chem. Res.* **1990**, *23*, 183-188.
- (11) Wang, Y.; Herron, N. *J. Phys. Chem.* **1991**, *95*, 525-532.
- (12) Stucky, G. D.; MacDougall, J. E. *Science* **1990**, *247*, 669-678.
- (13) (a) Choy, A.; Craig, D.; Dance, I. G.; Scudder, M. J. *Chem. Soc., Chem. Commun.* **1982**, 1246-1247. (b) Dance, I. G.; Choy, A.; Scudder, M. L. *J. Am. Chem. Soc.* **1984**, *106*, 6285-6295.
- (14) Hencher, J. L.; Khan, M. A.; Said, F. F.; Tuck, D. G. *Polyhedron* **1985**, *4*, 1263-1267.
- (15) Hagen, K. S.; Holm, R. H. *Inorg. Chem.* **1983**, *22*, 3171-3174.

[†] Universität Regensburg.

[‡] University of Texas.